Hetero-tandem organic solar cells drive water electrolysis with a solar-to-hydrogen conversion efficiency up to 10%

Young Kyeong Kim [a,1], Tack Ho Lee [b,1], Jiwoo Yeop [a], Woo Jin Byun [a], Jin Hyun Kim [a,*], Jin Young Kim [a,*], Jae Sung Lee [a,*]

[a] Department of Energy Engineering, School of Energy and Chemical Engineering, Ulsan National Institute of Science & Technology (UNIST), Ulsan 44919, Republic of Korea
[b] Department of Chemistry and Centre for Processable Electronics, Imperial College London, White City Campus, London W12 0BZ, UK

ARTICLE INFO

ABSTRACT

A hetero-tandem organic photovoltaic (OPV) device consisting of large (PM6:IT-M) and small-bandgap (PM6:Y6) bulk-heterojunctions is developed to provide an open-circuit voltage of 1.84 V and a power-conversion-efficiency of 11.7%, which could serve as an ideal light absorber to drive water electrolysis. The fabricated OPV is combined with an electrolyzer composed of $NiFeO_x(OH)_y$ and Pt electrocatalysts to demonstrate a photovoltaic-electrolysis (PV-EC) system. Furthermore, the system is designed to locate the operating voltage of the OPV-EC system at the maximum power point of OPV to minimize power loss. As a result, our hetero-tandem OPV-EC device achieves the highest solar-to-hydrogen conversion efficiency among OPV-based systems, (up to 10%), which represents a new benchmark for OPV-based solar fuel production. Finally, a wireless monolithic organic-artificial leaf is constructed for the first time, which demonstrates a stable solar hydrogen production in water.

1. Introduction

A sustainable solar-driven water electrolysis system for hydrogen production is required for a carbon-neutral society [1]. Solar energy could be directly converted to hydrogen through photocatalytic or photoelectrochemical water splitting [2]. However, these technologies are limited to laboratory scale, and their solar-to-hydrogen (STH) conversion efficiency is not sufficient for commercialization [3]. An alternative approach is the photovoltaic-electrolysis cell (PV-EC) system, which combines two independent technologies; power-providing PV and electrolysis induced EC, providing much higher STH efficiency than those of direct conversion processes [4].

Techno-economic analyses for solar hydrogen production show that the PV part is the most expensive and the performance-determining component for PV-EC systems [5,6]. Therefore, a high-performance PV manufactured at a low cost that can drive water electrolysis with sufficient STH efficiency is required to put the solar hydrogen production system into practical use [5]. Since the power conversion efficiency (PCE) of PV is a primary determinant of the STH efficiency of a PV-EC system, high STH efficiencies (as high as 30%) have been generally

reported for III-V semiconductor-based solar cells [7–9]. However, III-V light absorbers are not a suitable option because their widespread distribution is limited due to their scarcity and high manufacturing cost (> \$50/W) [10]. On the other hand, perovskites and their tandem PVs with other light absorbers have been applied to the PV-EC system due to their high PCEs and achieved STH efficiency of up to 18.7% [11,12]. Despite their excellent performance, the halide perovskites pose the major barriers to practical implementation, such as fast degradation within a few hours under illumination, and partially soluble in water leading to lead toxicity [13].

Organic photovoltaics (OPVs) are less efficient in general than conventional inorganic PVs, yet recent years have observed remarkable improvements in their PCEs [14]. Together with their well-known advantages such as low manufacturing costs and wide absorption ranges by tailoring molecular structures, the enhanced PCEs make OPV an attractive alternative to power the electrolysis cells [14–16]. Theoretically, a double-junction PV with an optical bandgap configuration around 1.80/1.20 eV is expected to maximize the efficiency of a PV-EC device by minimizing light utilization losses of the PV and power losses of the electrolyzer [17]. Thus, an OPV-EC system could be a

---

* Corresponding authors.
  E-mail addresses: kihi6783@unist.ac.kr (J.H. Kim), jykim@unist.ac.kr (J.Y. Kim), jlee1234@unist.ac.kr (J.S. Lee).
[1] These authors contributed equally to this work.

cost-effective option for solar hydrogen production if its STH efficiency arrives at 10%.

In this work, we fabricated a hetero-tandem OPV composed of two different sub-cells with a bandgap combination (1.61/1.37 eV) close to the theoretical optimum (1.8/1.20 eV), producing a photovoltage (V_{OC}) of 1.84 V suitable to drive water electrolysis. Our OPV-EC system employed Pt or NiMo/Ni foam and NiFeO$_x$(OH)$_y$/Ni foam for the hydrogen evolution reaction (HER) and oxygen evolution reaction (OER), respectively, in an alkaline electrolyte. Further, we designed to operate the system at 1.46 V, the maximum power point (MPP) of the OPV, by adjusting the area ratio of PV and EC to minimize the power loss. As a result, for the first time, we demonstrated the OPV-powered water electrolysis that recorded STH efficiency up to 10%, a new benchmark among reported OPV-EC systems. In addition, a wireless monolithic organic-artificial leaf was constructed for the first time, which demonstrated a stable solar hydrogen production in water.

2. Experimental methods

2.1. Preparation of Single PV cell

Through sequential ultrasonication treatment (distilled water, acetone, and isopropanol), the ITO substrates were cleaned. The ZnO precursor solution was prepared by mixing Tetrahydrofuran and diethylzinc in a 3:1 vol ratio. The prepared solution was spin-casted on the prepared substrate and then annealed under atmospheric conditions (120 °C for 10 min). The PM6:IT-M solutions were prepared with the same weight and then mixed with chlorobenzene:1,8-diiodooctane in a volume ratio of 100:1. The final solution has a concentration of 20 mg mL^{-1}. The PM6:Y6 solution was prepared by a 1: 1.2 wt ratio, and then blended in chloroform:1-chloronaphtalene in a volume ratio of 100:0.5. The ultimate solution has a concentration of 16 mg mL^{-1}. The PM6:IT-M or PM6:Y6 layer was spin-casted on top of the ZnO layer, and PM6:IT-M devices were annealed in a glove box filled with N$_2$ (100 °C for 10 min). Through the thermal evaporation, MoO$_3$/Ag electrodes were deposited with different thicknesses (5 and 80 nm) under vacuum ($<10^{-7}$ Torr) produced by a pump.

2.2. Tandem PV cell fabrication

As the front cell, ITO/ZnO/PM6:IT-M was prepared as described above. Through the thermal evaporation, the intermediate charge recombination layer was fabricated, under vacuum ($< 10^{-7}$ Torr) produced by a pump. After then, MoO$_3$/Au (15/1 nm) was deposited on top of the PM6:IT-M layer. On top of the MoO$_3$/Au, in sequence, ZnO nanoparticles synthesized according to a reported procedure were dispersed in methanol and deposited [18]. As the back cell, PM6:Y6/MoO$_3$/Ag was loaded on top of the MoO$_3$/Au/ZnO layer as previously described.

2.3. PV cell characterization

AM 1.5G illumination was used as a 1 sunlight source (100 mW cm^{-2}) and the characteristics of PV cells were measured inside the glove box filled with N$_2$ by using Keithley 2635A. The external quantum efficiency (EQE) measurements were carried out in ambient air. We used a QE system with monochromatic light.

2.4. Preparation of NiFeO$_x$(OH)$_y$ catalyst

Amorphous NiFeO$_x$(OH)$_y$ catalyst was prepared according to a reported procedure [19]. Through sequential ultrasonication treatment (hydrochloric acid, ethanol, and distilled water), FTO, Ni foil, and Ni foam were cleaned. Ni and Fe precursor solutions were prepared in 0.2 M by dissolving of Nickel(II) nitrate hexahydrate and Iron(III) nitrate nonahydrate into 2-methylethanol. Ni and Fe solutions were blended

into a molar ratio of 2:8. The 40 μL cm^{-2} of the prepared solution was drop-casted onto a Ni foam, and then, dried in an oven. After drying, the electrode soaks in alkaline solution to precipitate transition metal hydroxide on the surface of the substrate less than 10 s the remained KOH solution washed away with deionized water and ultimately NiFeO$_x$(-OH)$_y$ film was prepared by applying a potential range from 0.8 to 1.8 V vs. RHE under ambient states.

2.5. Preparation of NiMo catalyst

The NiMo catalyst was prepared via the electrodeposition method following the literature [20]. After cleaning the Ni Foam and foil substrates in the same way as above, they were manufactured in the form of electrodes. 3.154 g of NiSO$_4$·6H$_2$O (Sigma-Aldrich, 95.8–102.0%), 1.946 g of NaMoO$_4$·2H$_2$O (Sigma-Aldrich, > 99.5%), and 3.529 g of Na$_3$C$_6$H$_5$O$_7$·2H$_2$O (Sigma-Aldrich, > 99%) were dissolved in 120 mL of NH$_4$OH (Sigma-Aldrich, > 99.5%) to make a deposition solution. NiMo film was prepared by applying cathodic current density (-160 mA cm^{-2} for 900 s) in ambient states.

2.6. Preparation of Pt catalyst

Through spontaneous galvanic replacement, Platinum was loaded on the Ni metal substrates [21]. First, PtCl$_6$$^{2-}$ ion in the solution diffused to the surface of Ni electrode and adsorbed. Next, Oxidation of Ni on the electrode surface and reduction of Pt^{4+} provided from PtCl$_6$$^{2-}$ proceed simultaneously. As a result, the oxidized Ni is dissolved in the electrolyte and Pt exists as a metal on the electrode surface. ($2Ni(s) + Pt^{4+} \rightarrow Pt(s) + 2Ni^{2+}$) [22]. 243.94 μL of H$_2$PtCl$_6$ (Sigma-Aldrich, 8 wt%) and 49.76 mL of 0.01 M HCl (Sigma-Aldrich) were mixed to make a deposition solution. Ni foam and Ni foil were immersed in the solution at 600 rpm at ambient conditions for 30 min, washed with deionized water, and used as electrodes.

2.7. Physical characterization

The surface morphology was obtained from a field-emission SEM by Hitachi High-Technologies (S-4800). UV–vis absorption and spectrometer were recorded on a Perkin Elmer's Lambda 950. X-ray diffraction (XRD) patterns were profiled on with Cu−Kα radiation sources (λ = 1.54056 Å). XPS (ThermoFisher, Kα) analysis was used to shed light on surface atomic composition and determine the electrochemical states of each element. The overall water splitting test was initiated, and gas chromatography (GC-HP 7890) analysis was conducted to analyze the evolved hydrogen and oxygen gas, using a packed column (Supelco, Caboxen 1000).

2.8. Measurements of electrochemical performance

All of the Electrochemical performances were measured through a potentiostat (Ivium technologies) and the half-catalyst performance (HER and OER) of each sample was analyzed in a three-electrode cell setup. The prepared sample is working, Pt wire is counter, and Hg/HgO (1.0 M NaOH) served as reference electrodes. The LSV tests were performed under the same conditions (scan rate of 10 mV s^{-1} under stirring). Utilizing the Nernst equation as follows: $E_{RHE} = E(Hg/HgO) + 0.059 pH + 0.118$, where potentials were referenced to reversible hydrogen electrode (RHE) without iR compensation. For overall water electrolysis, a two-electrode configuration was employed. Unless otherwise noted, all electrodes had a size of 2.0 cm^2 and are measured in alkaline media (1.0 M KOH; pH 13.6).

2.9. Operation of OPV-EC system

A solar simulator (91160, Oriel) and potentiostat were used to

irradiate the light into the OPV-EC system and measure its electrochemical performance. Before all-optical measurements, the irradiated light was calibrated with 1 sun condition (100 mW cm^{-2}). To operate the OPV-EC system, the negative part of the OPV from which electrons come out is connected to the cathode to induce a reduction reaction (HER), and the positive part of the OPV where electrons enter is connected to the anode to induce an oxidation reaction (OER). The potentiostat wedge between the OPV-EC systems along with the flow of electrons to measure the electrochemical performance of the above system. The potentiostat working electrons (electron acceptor) and counter electrodes (electron donor) was connected to the negative part of the OPV and the cathode, respectively. For the stability test, the OPV was encapsulated by the transparent glass using epoxy resin and their performance was measured under either simulated sunlight provided by a solar simulator or visible light illumination with a 420 nm cut-off filter.

3. Results and discussion

3.1. Hetero-tandem organic solar cells

The characteristic of OPV materials to fabricate the tandem cell, including chemical structures, absorption spectra, and energy levels, are demonstrated in Fig. 1. The full name of organic materials (PM6, IT-M, and Y6) are detailed in Supplementary Information (SI). PM6 is a polymer donor with a wide-bandgap and its bulk-heterojunction (BHJ) with a near-infrared absorbing non-fullerene acceptor (NFA) is widely used as an efficient OPV by virtue of widened absorption ranges and reduced energy losses compared to fullerene-based OPVs [23,24]. To our best knowledge, NFA-based tandem cells have not yet been used for water electrolysis, while previous OPV-EC systems employed side-by-side connected PV configurations or fullerene-based homo tandem cells (This will be discussed in detail later). IT-M is a methyl-end-capped NFA, which has elevated energy levels by the electron-donating methyl group to increase the V_{OC} of OPVs [25]. In

general, IT-M based single-junction PVs have V_{OC} around 1 V, indicating that IT-M is a promising NFA to be used in a sub-cell of the high photovoltage tandem cell [26]. As a low bandgap NFA, Y6 can absorb the light up to 1000 nm wavelength. PM6:Y6 BHJ is a well-known highly efficient OPV for providing a short-circuit current density (J_{SC}) greater than 20 mA cm^{-2} by covering a wide range of photon harvesting and high a PCE approaching 18% [27].

The back cell in the tandem cell can absorb the light that transmits through the front cell, thus the PM6:Y6 BHJ has a great advantage as a back cell of the tandem cell owing to its high absorption onset wavelength (λ_{onset}). Thus, we chose PM6:IT-M and PM6:Y6 as the front and back cells, respectively, to optimize the J_{SC} and V_{OC} of our tandem OPV device. Two-terminal, series-connected tandem cells were fabricated and it has an architecture of indium tin oxide (ITO)/ZnO/PM6:IT-M/MoO$_3$/Au/ZnO/PM6:Y6/MoO$_3$/Ag to achieve a high photovoltage suitable for overall water splitting (Figs. 1c and 2a). Further, the inverted architecture was selected with metal oxide interlayers and the MoO$_3$/Au/ZnO intermediate recombination layer between front and back cells to avoid using water-soluble interlayers (e.g. PEDOT:PSS) [28]. The fabrication process is detailed in the Experimental Methods.

Fig. 2b describes the PCE of the tandem cell estimated as a function of λ_{onset} of the front and the back cells according to the method described in SI. The optimal PCE is 18.2% with λ_{onset} of ideal front and back cells of 690 and 910 nm, respectively, assuming a fill-factor of the tandem cell to be 0.70. Fig. 2c demonstrates the absorption spectra of the front (PM6:IT-M) and.

the back (PM6:Y6) films, and the EQE spectra of the PM6:IT-M and the PM6:Y6 single-junction PV. Since λ_{onset} of PM6:IT-M and PM6:Y6 is 770 and 900 nm, respectively, the PCE of the tandem cell is estimated as 13.3% from our model in Fig. 2b. The absorption width was further confirmed with the total reflectance of the tandem cell in Fig. S1. The current density-voltage (J-V) curves of single-junction and tandem cells are depicted in Fig. 2d, and the corresponding PV parameters are summarized in Table S1. PM6:IT-M devices exhibited high V_{OC} approaching
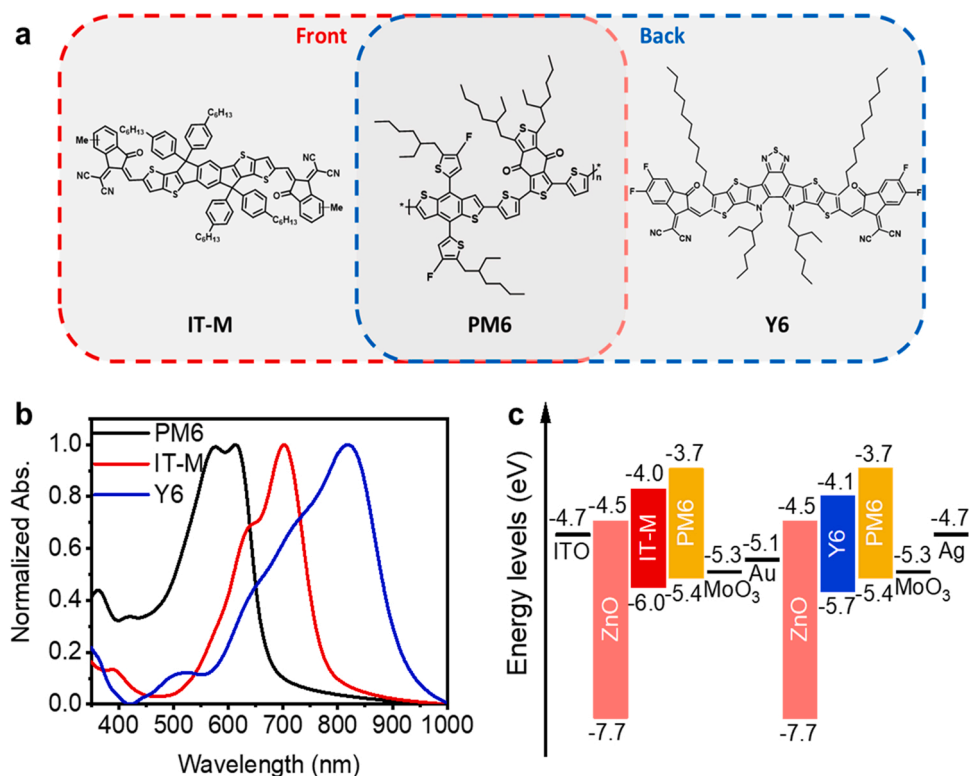

Fig. 1. Material design and characterization of OPV. (a) Molecular structures, (b) normalized absorption spectra of OPV materials, and (c) energy levels of the tandem cell.
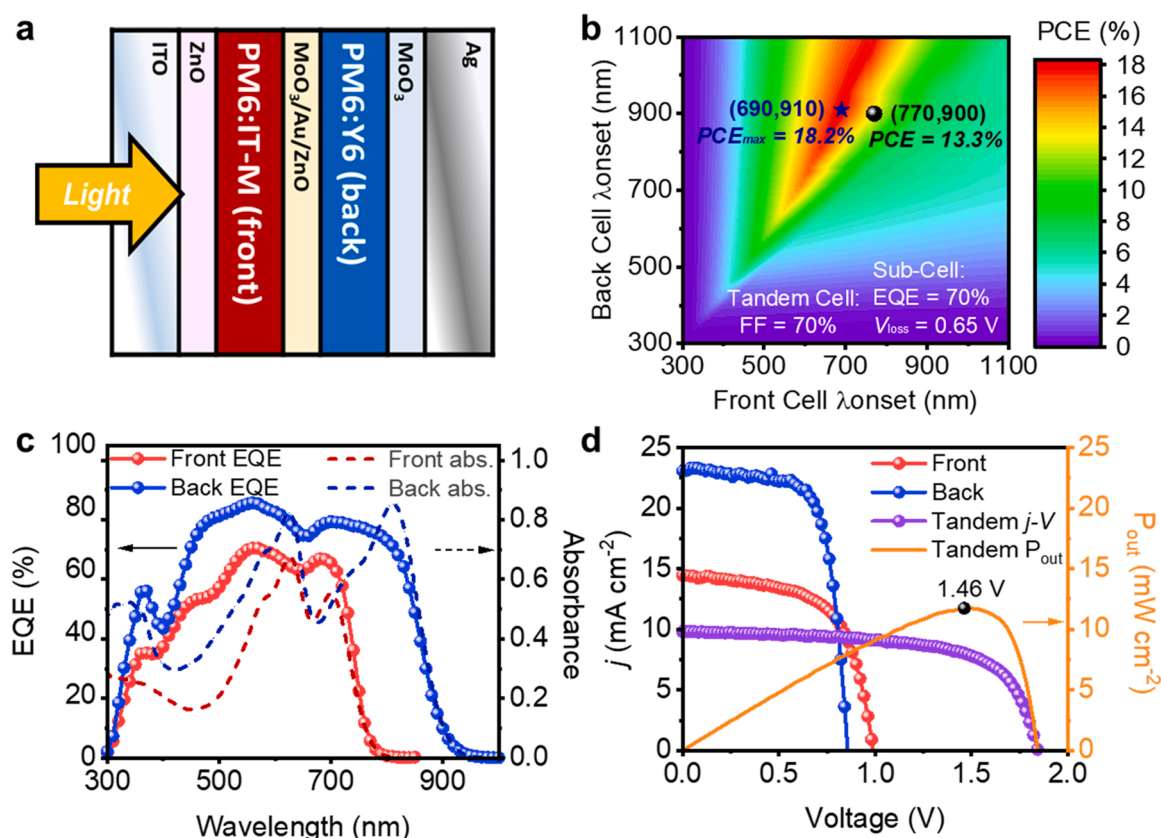
Fig. 2. Photovoltaic performance of OPV. (a) Schematic diagram of the tandem cell. (b) Estimation of tandem cell PCE as a function of the front and the back cell absorption onset. (c) Absorption spectra (dashed lines) and EQE (filled circles) of the PM6:IT-M (front) and the PM6:Y6 (back) cell. (d) *J-V* curves of the sub-cells and the tandem cell, and the output power density (P_{out}) curve of the tandem cell. The voltage at the MPP of the tandem cell is 1.46 V.

1 V with their onset below 800 nm and PM6:Y6 devices demonstrated J_{SC} of 23.1 mA cm^{-2} with their onset around 900 nm, indicating that PM6:IT-M and PM6:Y6 PVs are suitable for the front and the back cells of our tandem OPV cell as we expected. As a result, the PM6:IT-M/PM6:Y6 tandem cell exhibited V_{OC} of 1.84 V and J_{SC} of 9.81 mA cm^{-2} and demonstrated PCE of 11.7%. Our optimized tandem cell achieved the PCE approaching 90% of the calculated PCE of 13.3%. It is noteworthy that the operating area of our OPVs is 0.56 cm^2 to match with the operating area of ECs for overall water splitting, which is a rather large area relative to generally reported high-efficiency OPVs. The V_{OC} of the tandem cell is almost identical to the sum of V_{OC}s of the two sub-cells, indicating our tandem architecture minimizes V_{OC} losses caused by the series-connection of two sub-cells. By virtue of the high V_{OC} of 1.84 V, the voltage at the MPP of the tandem cell is 1.46 V (Fig. 2d), which is a feasible voltage to drive the overall water electrolysis. In view of PV performance only, the overall PCE of our tandem OPV is lower than that of PM6:Y6 single-junction PV. However, we designed our tandem OPVs to achieve the high V_{OC} of 1.84 V suitable for powering water-splitting reactions in the OPV-EC system. Hence, our hetero-tandem OPV has features tailor-made for the PV-EC application.

3.2. Electrochemical performance of catalysts for water splitting

To produce low-cost hydrogen through PV-EC devices, reducing overpotentials of water splitting by applying efficient and low-cost electrocatalysts is required [6]. Pt was chosen as the hydrogen evolution catalyst (HEC) due to its high HER catalytic performance and the low-cost NiMo catalyst was also prepared to compensate for the high cost of Pt [29,30]. For the oxygen evolution catalyst (OEC), NiFe oxyhydroxide (NiFeO$_x$(OH)$_y$), which is a representative non-precious metal catalyst of excellent OER performance comparable to noble metals in a

basic solution, was selected [31]. (See experimental methods for details).

The electrocatalytic properties of each catalyst coated on different substrates were investigated by cyclic voltammetry (CV) and linear sweep voltammetry (LSV) (Fig. S2 and S3). Among the three different substrates, Ni foam has the highest electrochemical surface area (2.93 mF cm^{-2}) compared to Ni foil and fluorine-doped tin oxide (FTO). Furthermore, Ni foil and Ni foam showed distinct OER activity with an oxidation peak at 1.40 V_{RHE}, which is originated from the oxidation of Ni species, indicating that Ni on the substrate itself can act as an electrocatalyst [32]. Thanks to these advantages, The LSV curves of NiFeO$_x$(OH)$_y$, Pt, and NiMo show the highest catalytic performances on the Ni foam. Hence, in this work, all catalytic performances of each catalyst were observed on the Ni foam. The optimization of the synthesis conditions to obtain best catalytic performance is described in Fig. S4. NiFeO$_x$(OH)$_y$/Ni foam shows the highest OER performance when Ni and Fe metal molar ratio is 2:8, and the HER performances of Pt and NiMo/Ni foam are saturated when the galvanic exchange and electrochemical deposition times exceed 30 min and 900 s, respectively. Hence, all electrode catalysts used in PV-EC systems were synthesized under these optimized conditions hereafter.

Further physico-chemical analysis of each catalyst was performed to determine the structural and compositional properties (Fig. S5-S7). The scanning electron microscope (SEM) images show that each catalyst is uniformly deposited on the substrate. X-ray diffraction (XRD) patterns are dominated by the underlying Ni foam substrate because the amount of deposited catalyst is smaller than that of Ni foam. X-ray photoelectron spectroscopy (XPS) confirms the presence of each element in its expected oxidation state.

In Fig. 3a, to reach 10 mA cm^{-2}, the NiFeO$_x$(OH)$_y$/Ni foam needs an overpotential (η_{OER}) of only 220 mV and it is 80 mV lower than that of
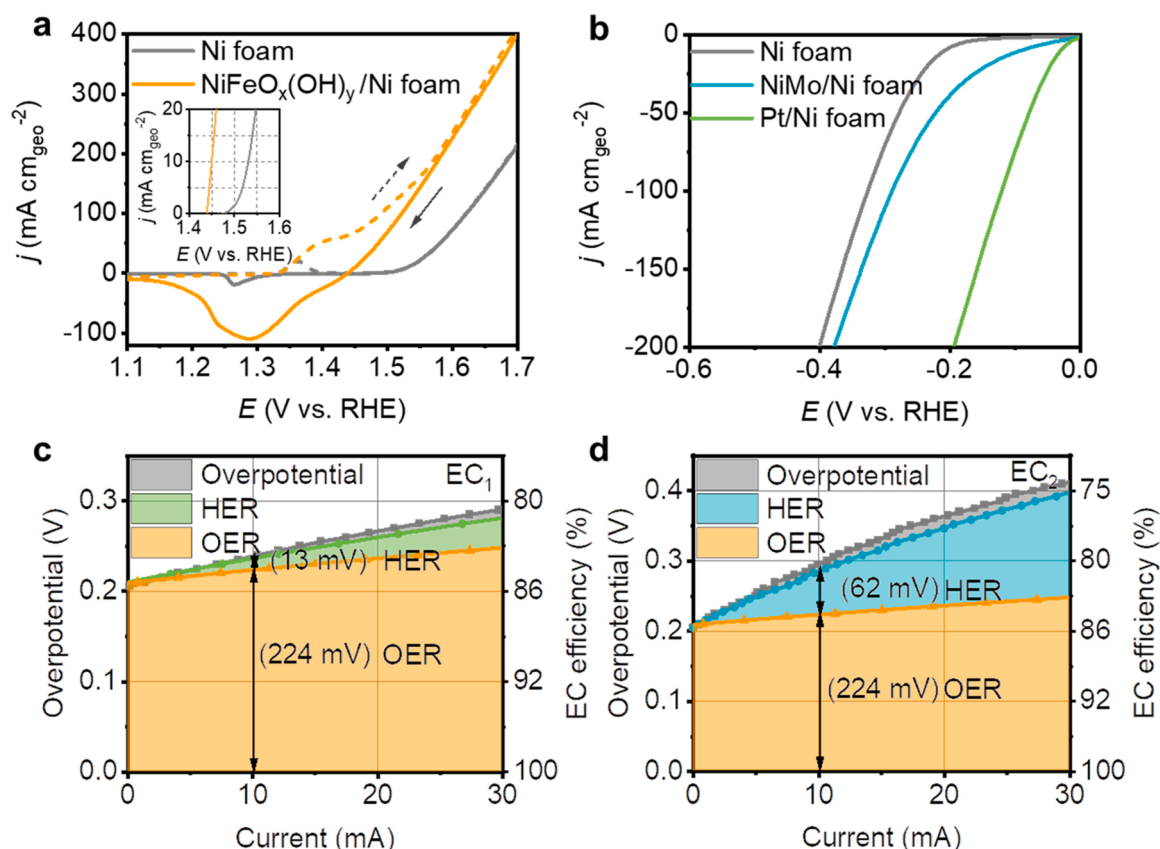
Fig. 3. Overall water-splitting performance of electrocatalysts. (a) LSV curves of NiFeO$_x$(OH)$_y$/Ni foam for OER in forward (dashed line) and reverse direction (solid line) and (b) Pt/Ni foam and NiMo/Ni foam for HER compared to bare Ni foam. (c) Decoupled overpotential of overall water splitting reaction and electrochemical cell efficiency (η_{cell}) of EC$_1$: NiFeO$_x$(OH)$_y$/Ni foam (anode) || Pt/Ni foam (cathode) and (d) EC$_2$: NiFeO$_x$(OH)$_y$/Ni foam (anode) || NiMo/Ni foam (cathode) in a two-electrode configuration.

the bare Ni foam (see inset). The LSV curves were scanned in the reverse direction to exclude the effect of the pre-oxidation peak attributed to the Ni^{2+}/Ni^{3+} redox cycle [33]. In Fig. 3b, the Pt/Ni foam and the NiMo/Ni foam required overpotentials (η_{HER}) of 30 and 91 mV at 10 mA cm^{-2}, respectively, which are much smaller than.

that of bare Ni foam (208 mV). The Tafel plots in Fig. S8a show that NiFeO$_x$(OH)$_y$/Ni foam displays a lower Tafel slope (42.5 mV dec^{-1}) than that of Ni foam (56.4 mV dec^{-1}) in OER. Among the HER electrocatalysts, Pt/Ni foam has the lowest Tafel slope of 52.9 mV dec^{-1}, while NiMo/Ni foam and Ni foam show 167.8 mV dec^{-1} and 94.5 mV dec^{-1}, respectively (Fig. S8b). Electrochemical impedance spectroscopy (EIS) was measured to study interfacial charge transfer properties between electrolyte and electrode. Fig. S9 shows the Nyquist plot of OER and HER electrocatalysts measured at an overpotential of 320 mV and 50 mV, respectively. The charge transfer resistances (R$_{ct}$) of NiFeO$_x$(OH)$_y$, NiMo, and Pt on Ni foam are significantly lower than that of bare Ni foam, indicating their fast charge transport during the OER and HER processes. Although the performance of the NiMo/Ni foam is lower than that of the Pt/Ni foam, the cost advantage of the NiMo catalyst could offset its higher overpotential at a practical scale.

Adjusting the area ratio of EC and PV (A$_{EC}$/A$_{PV}$) is a practical strategy to lower the voltage required to drive the PV-EC system, and thereby minimize the power loss [9]. To figure out the optimized A$_{EC}$/A$_{PV}$, we investigated the electrocatalytic performance of each catalyst according to the size of the electrode area (A$_{EC}$) (Fig. S10 and S11). As the A$_{EC}$ increases from 0.25 to 9.00 cm^2, the HER and OER catalytic current increases linearly, which is beneficial for reducing the voltage required for EC operation [9]. The catalytic current of EC$_1$ (NiFeO$_x$(OH)$_y$ /Ni foam || Pt/Ni foam) and EC$_2$ (NiFeO$_x$(OH)$_y$ /Ni foam|| NiMo/Ni foam) also increases with the A$_{EC}$ but at the voltage near 1.46 V (MPP of the

OPV), the electrode over 2.00 cm^2 has a saturated current. Therefore, we consider that 2.00 cm^2 electrode is an optimum size to deliver the power provided by the OPV. Fig. 3c and d display decoupled overpotentials of the optimized EC$_1$ and EC$_2$ (A$_{EC}$ = 2.0 cm^2) into η_{HER}, η_{OER}, and ohmic losses (η_{ohm}) including ohmic resistance, kinetics, and local hydroxide mass transfer [34]. The total overpotentials of EC$_1$ and EC$_2$ are only 240 and 295 mV at 10 mA, respectively, and the electrochemical cell efficiency (η_{Cell}) can be calculated based on these experimental values by the method described in SI. The calculated η_{Cell} of EC$_1$ and EC$_2$ is 83.7% and 80.6% at 10 mA, representing their excellent efficiency in converting electrical energy into hydrogen fuel.

The durability of our ECs was tested by applying a current density of 100 mA cm^{-2} consistently for 24 h (Fig. S12). The required voltage of EC$_1$ and EC$_2$ increase by only 1.7% and 1% for 24 h demonstrating the remarkable stability of both cells. Since our OPV-EC system operates in milder conditions ($<$ 10 mA cm^{-2}, see next section), the observed deactivation of our ECs at such a high current density (100 mA cm^{-2}) could be considered insignificant. The SEM image after the durability test confirmed that there was no significant catalyst morphology change, and all catalysts remained adhered well to the electrode (Fig. S13). In addition, XPS analysis revealed that all elements were well maintained in the catalyst (Fig. S14). The only noticeable change was that the intensity of the O1s peak increased, indicating that the catalyst surface was oxidized during the OER reaction. During the stability test, we measured the amount of H$_2$ and O$_2$ by gas chromatography and confirms a 2:1 molar ratio with a faradaic efficiency close to 100%, indicating that EC systems have no significant loss of electricity and gaseous products (Fig. S15).

3.3. Water splitting powered by hetero-tandem organic solar cells

A solar-driven water electrolysis system was realized by combining the hetero-tandem OPV and the electrolyzer either EC_1 or EC_2 (Fig. 4a). The combined OPV-EC system operates when the current and voltage between the two systems are equal. Therefore, the operating point is defined as the point where the *J-V* curves of OPV and EC intersect, and the current density and voltage at this point are called the operating current density (J_{op}) and voltage (V_{op}). Adjusting this operating point to coincide with the MPP of OPV (1.46 V) allows the generated power to be fully transferred to EC with a minimal loss [9]. We investigated how the operating point of OPV-EC varied with the electrode area (A_{EC}) from 0.25 to 9.0 cm^2 for a fixed OPV area (A_{PV} = 0.56 cm^2). Fig. S16 represents that the operating point of the OPV-ECs approaches 1.46 V as A_{EC} increases, confirming that adjusting the A_{EC}/A_{PV} ratio can tune the operating point of OPV-EC system. The matching efficiency (η_{op}) between PV and EC system is one of the parameters that can numerically guide the system optimization (as described in SI). As shown in Table S4, the η_{op} of OPV-EC$_1$ and OPV-EC$_2$ reached 100% and 99.5%, respectively, when the A_{EC}/A_{PV} ratio was 3.6 (A_{EC} = 2.0 cm^2).

By achieving 100% of η_{op} in the optimized OPV-EC$_1$ system, the only wasted power is the kinetic loss (P_{kin}) due to the overpotential of water electrolysis. Unlike conventional PV-EC systems, which manipulate the V_{op} using a DC-DC converter with extra power, cost, and space, we optimized system design simply by adjusting the A_{EC}/A_{PV} ratio [9].

The LSV curves of an optimized OPV-EC$_1$ are shown in Fig. 4b. The OPV-EC$_1$ system shows a J_{op} of 8.2 mA cm^{-2} at 1.46 V, giving an STH

efficiency of 10%. It indicates that the electricity generated by OPV (PCE = 11.7%) is converted into hydrogen fuel (STH = 10%) by EC$_1$ with an electrochemical conversion efficiency (STH/PCE = η_{EC}) of 85%. The performance of the combined OPV-EC$_1$ system was further investigated by scanning the LSV curves scanning from − 1.0 to 0.5 V in Fig. 4c. At 0.0 V where no external bias is applied, the OPV-EC$_1$ device generates a J_{op} of 8.0 mA cm^{-2}, corresponding to STH of 9.8%, reflecting a small connecting loss in the real OPV-EC system [35]. The OPV-EC$_2$ system operates at 1.50 V, slightly higher than the MPP of OPV due to the higher η_{HER} of NiMo compared to that of Pt, and exhibits a J_{op} of 7.8 mA cm^{-2} (Fig. S17). As a result, OPV-EC$_2$ has an expected STH efficiency of 9.6% and η_{EC} of 82.1%, owing to the coupling loss originating from the system mismatch.[36]. In an actual OPV-EC$_2$ system operation, the J_{op} was 7.1 mA cm^{-2} corresponding to an STH efficiency of 8.7%.

A chronoamperometric test of the OPV-EC systems at 0.0 V was conducted for 600 s to determine its stability (Fig. 4d and S17c). Under an AM 1.5G chopped light illumination, the OPV-EC$_1$ and OPV-EC$_2$ systems maintain 98.8% and 85.0% of the initial STH efficiency for 600 s, whereas their performance decreased to 80.8% and 51.6% when the operation was extended to 2 h (Fig. S18). Despite the superior stability of electrolyzers (Fig. S12), photocurrent density shows a gradual decrease during the operation of the OPV-EC system, indicating that the OPV is deactivated over time and induces a decrease in the efficiency of the entire system. OPVs are known to be susceptible to UV light and moisture since UV light can induce photo-degradation of OPVs and the ingress of ambient oxygen is detrimental to the device performance [37–39]. In particular, the donor:acceptor blended active layer of OPVs
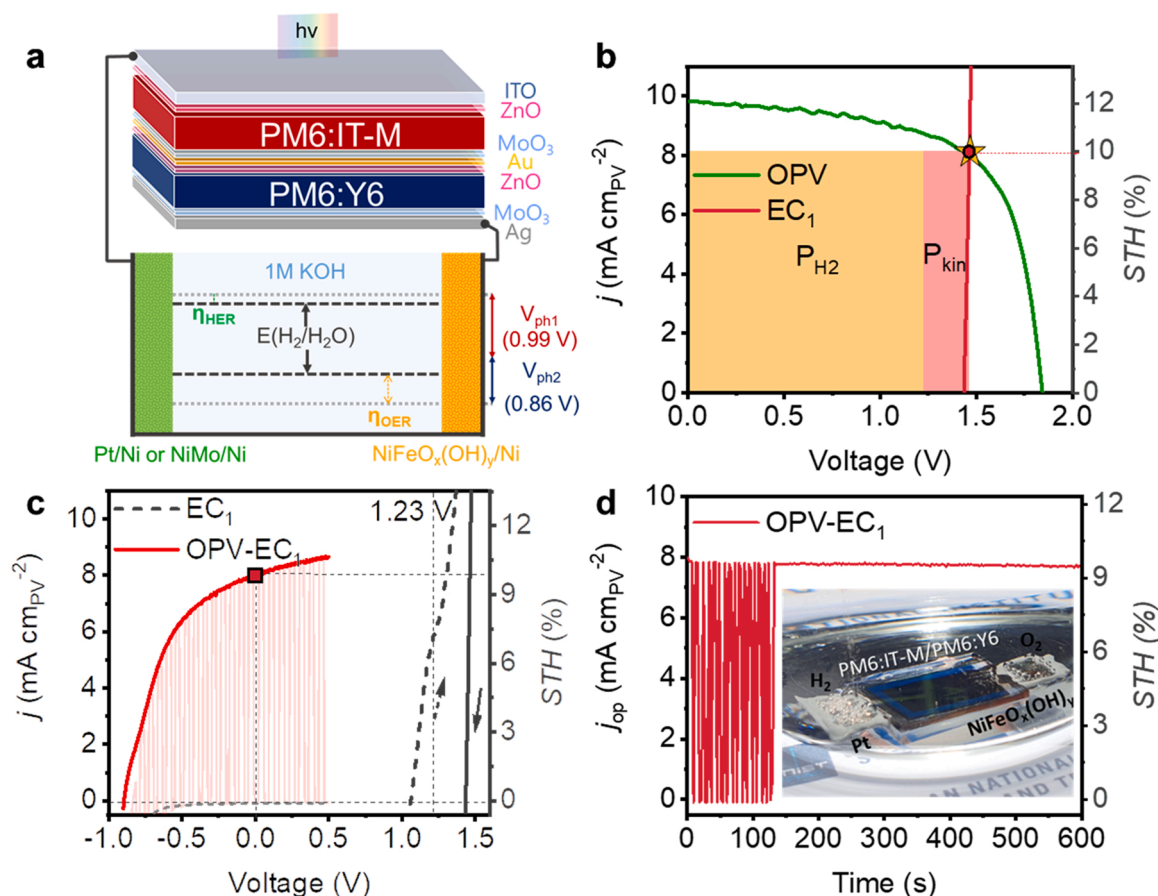

Fig. 4. PM6:IT-M/PM6:Y6 tandem OPV-EC for water splitting. (a) Schematics of the OPV-EC system. (b) LSV of OPV (0.56 cm^2) and EC$_1$ in a two-electrode configuration (2.0 cm^2). The MPP of PV and the operating point of EC$_1$ are marked with a star and a dot, respectively. The amount of power stored as hydrogen (P_{H2}) and that wasted as kinetic loss (P_{kin}) are indicated. (c) LSV of EC$_1$ in a two-electrode configuration and OPV-EC system with its STH efficiency. (d) The current density generated by the OPV-EC$_1$ system without external bias (applied bias = 0.0 V). The inset is the photograph of a wireless, monolithic OPV-EC$_1$ device (organic artificial leaf) conducting overall water splitting under simulated 1 sun.

has inherently weak morphological stability, showing photodegradation by severe donor/acceptor phase separation [40]. It should be noted that all measurements of our OPV-EC systems were carried out without any encapsulation of OPV, thus directly exposed to ambient air (oxygen and humidity) under 1 sun illumination. Cutting the UV light in the illumination is a well-known strategy that can improve the photo-stability of OPVs [41,42]. Indeed, the stability of OPV-EC$_1$ and OPV-EC$_2$ improved to 81.9% and 71.4% when their performance was measured under the visible light irradiation with a 420 nm cut-off filter (Fig. S19). Furthermore, when OPV was encapsulated with glass using transparent epoxy resin to prevent the penetration of oxygen and water, both OPV-EC systems show a huge stability improvement up to 92.8% and 90.6%, respectively, under an AM 1.5G light illumination. This indicates that the primary reason for the destabilization of the OPV-EC system is the oxygen/moisture exposure of OPV, which accelerates photo-oxidation of the active layer [43]. Finally, when the two strategies were adopted in combination, the initial activities of encapsulated OPV-EC$_1$ and OPV-EC$_2$ were maintained up to 96.4% and 95.0% under visible light irradiation.

Furthermore, we explored the feasibility of an 'organic artificial leaf' that mimics natural photosynthesis by wirelessly combining our OPV and catalysts (Fig. S20). Such a device was first demonstrated by Reece et al. using a triple-junction amorphous Si solar cell combined with OEC (Co-Bi)/HEC (NiMoZn) [44]. This stand-alone device can drive water splitting directly without the use of external wires and has an advantage for applications due to its mobility, flexible scale, and simple design [45]. The specific fabrication process is described in SI. The wireless organic artificial leaf has a configuration of Pt(HEC)/Ni/Cu––ITO/ZnO/PM6:IT-M/MoO$_3$/Au/ZnO/PM6:Y6/MoO$_3$/Ag–Cu/Ni/NiFeO$_x$(OH)$_y$(OEC), and photo-induced electrons are transferred from the front cell (PM6:IT-M) to the cathode electrode (Pt/Ni foil) through the directly-connected charge collector (Cu tape) to generate H$_2$ gas. On the other side, photo-induced holes migrate from the back cell (PM6:Y6) to the anode (NiFeO$_x$(OH)$_y$/Ni foil) to produce O$_2$ gas.

This organic artificial leaf was operated under AM 1.5G solar irradiation in 1.0 M KOH electrolyte, and the continuous electrolysis water. At each electrode, the generation of hydrogen and oxygen bubbles was easily observed by the naked eye over 1 h, demonstrating the robustness of our organic artificial leaf (Fig. S15c-S15d, inset of Fig. 4d, and Supplementary Video).

Supplementary material related to this article can be found online at doi:10.1016/j.apcatb.2022.121237.

3.4. Benchmarking OPV-powered water electrolysis systems

We summarize STH efficiency and η_{EC} values of OPV-EC systems reported in the literature in Fig. 5 and Table S2 in SI, by classifying them according to the OPV configuration. Esiner et al. [46] and Wu et al. [47] investigated an OPV-EC system with a side-by-side connected OPV and alkaline electrolyzer achieving an STH efficiency of 6.1% and 6.15%, respectively. On the other hand, Gao et al. [48] and Esiner et al. [49] combined the double-junction tandem OPV of two identical sub-cells with an alkaline electrolyzer to record an STH efficiency of 6.1%. The triple-junction tandem OPVs using either identical or different light absorbers yielded lower STH efficiencies than those of the double-junction OPV (~6.1%), [50–52] because they provide excessive V_{OC} over 2 V, leading to a higher system energy loss.

Compared to these previous OPV-EC systems, the most ingenious feature of our system is the adoption of hetero-tandem OPV using dual light absorbers with near-ideal bandgap alignment. Thus, two bulk heterojunctions that have a bandgap alignment of 1.61/1.37 eV are close to the ideal combination (1.80/1.20 eV) that gives theoretically the highest STH efficiency [17]. Our hetero-tandem OPV generated an optimized voltage (V_{OC} = 1.84 V) suitable for water splitting, and J_{SC} of 9.81 mA cm^{-2} with PCE of 11.7%. Furthermore, we employed the design strategy to minimize the energy loss between PV and EC by manipulating the A$_{EC}$/A$_{PV}$ ratio. Finally, efficient electrocatalysts were employed for the electrolyzer composed of NiFeO$_x$(OH)$_y$/Ni foam and Pt/Ni foam to obtain η_{EC} of 85.5%, which is close to the theoretical limit [53,54]. As a result, our OPV-EC$_1$ system achieved the STH efficiency up to 10%, which sets a new benchmark in water electrolysis using an OPV-EC system. In addition, the OPV-EC$_2$ system yields an STH efficiency of 9.6% even without using noble metal. Furthermore, we summarize the STH efficiency and η_{EC} of the recently reported PV-EC systems powered by different types of PVs in Fig. S21 and Table S3.
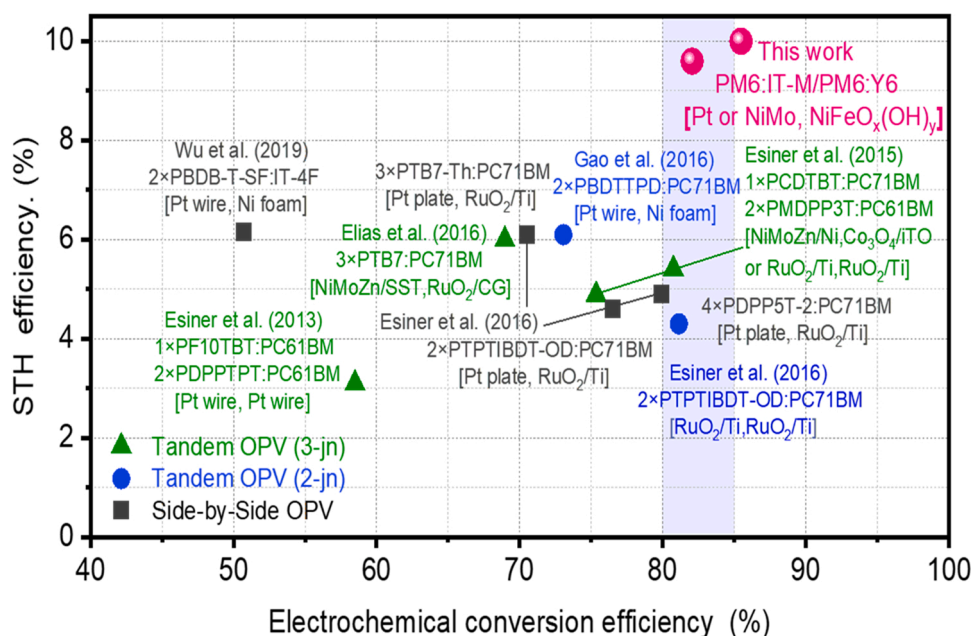

Fig. 5. STH efficiency and electrochemical conversion efficiency benchmark for OPV-EC systems. Details of the references can be found in Table S2, and in the main text. The systems were classified according to the configuration of OPV used in the system (Side-by-side OPV,[46,47] tandem OPV (2-jn), [48,49] and tandem OPV (3-jn) [50–52]).

Although the STH efficiencies of OPV-EC systems are much lower than those based on expensive III-V compound PVs, the performance of our hetero-tandem OPV-EC system is competitive with those based on extensively-studied Si and perovskite PVs.

4. Conclusions

For the first time, we demonstrated an OPV-powered overall water electrolysis system with an STH efficiency up to 10%, which has been considered as the milestone for practical solar hydrogen production. To achieve this, we successfully optimized hetero-tandem organic light absorbers with a combination of large-bandgap PM6:IT-M as the front and small-bandgap PM6:Y6 as the back cell, which generated V_{OC} of 1.84 V and J_{SC} of 9.81 mA cm^{-2} and achieves a PCE of 11.7%. Combining with an alkaline electrolyzer composed of NiFeO$_x$(OH)$_y$ and Pt as OEC and HEC, respectively, a new benchmark of STH efficiency (10%) and an electricity-to-hydrogen conversion efficiency (η_{EC}) (84.5%) was achieved. Even with non-precious metal-only electrocatalysts of NiFeO$_x$H$_y$ and NiMo, similar STH efficiency of 9.6% and η_{EC} of 81.8% were obtained. From a fundamental point of view, the OPV-EC system consisting of hetero bandgap light absorbers (dual light absorbers) – four-photon approach has never been realized before. In addition, we were able to minimize the energy loss between PV and EC by manipulating the A$_{EC}$/A$_{PV}$ ratio and employing efficient electrocatalysts for overall water splitting.

This work demonstrates that the hetero-tandem OPV could be a promising candidate for powering PV-driven water splitting systems for practical solar hydrogen production. Considering the recent rapid development of highly efficient OPVs, their application to solar hydrogen production will receive increasing attention. Especially promising research topics could be developing organic semiconductor materials of the near-ideal optical bandgap combination and improving the stability of solar cells. If we consider the low cost and scalability of OPV in general, we can say that the prospect for OPV-EC to produce solar hydrogen on large scales is highly promising with further developments.

CRediT authorship contribution statement

Jae Sung Lee, **Jin Young Kim**, and **Jin Hyun Kim** proposed, designed, and directed the project. **Tack Ho Lee** with the help of **Jiwoo Yeop** prepared and characterized the organic photovoltaic cells. **Young Kyeong Kim** and **Jin Hyun Kim** performed the synthesis and analysis of electrocatalysts. **Woo Jin Byun** performed Faradaic efficiency measurements. **Young Kyeong Kim** and **Jin Hyun Kim** devised optimized OPV-EC systems and measured their performances. **Tack Ho Lee** and **Jiwoo Yeop** promote the concept of stabilizing organic photovoltaic cells. **Young Kyeong Kim**, **Tack Ho Lee**, **Jin Hyun Kim**, **Jin Young Kim**, and **Jae Sung Lee** discussed the results and wrote the paper.

Declaration of Competing Interest

The authors declare that they have no known competing financial interests or personal relationships that could have appeared to influence the work reported in this paper.

Acknowledgments

Appendix A. Supporting information

Supplementary data associated with this article can be found in the online version at doi:10.1016/j.apcatb.2022.121237.

References

[1] J.H. Kim, D. Hansora, P. Sharma, J.-W. Jang, J.S. Lee, Toward practical solar hydrogen production – an artificial photosynthetic leaf-to-farm challenge, Chem. Soc. Rev. 48 (2019) 1908–1971.

[2] D.G. Nocera, The artificial leaf, Acc. Chem. Res. 45 (2012) 767–776.

[3] M. Grätzel, Photoelectrochemical cells, Nature 414 (2001) 338–344.

[4] T.J. Jacobsson, V. Fjällström, M. Edoff, T. Edvinsson, Sustainable solar hydrogen production: from photoelectrochemical cells to PV-electrolyzers and back again, Energy Environ. Sci. 7 (2014) 2056–2070.

[5] B.A. Pinaud, J.D. Benck, L.C. Seitz, A.J. Forman, Z. Chen, T.G. Deutsch, B.D. James, K.N. Baum, G.N. Baum, S. Ardo, H. Wang, E. Miller, T.F. Jaramillo, Technical and economic feasibility of centralized facilities for solar hydrogen production via photocatalysis and photoelectrochemistry, Energy Environ. Sci. 6 (2013) 1983–2002.

[6] C.A. Rodriguez, M.A. Modestino, D. Psaltis, C. Moser, Design and cost considerations for practical solar-hydrogen generators, Energy Environ. Sci. 7 (2014) 3828–3835.

[7] J. Jia, L.C. Seitz, J.D. Benck, Y. Huo, Y. Chen, J.W.D. Ng, T. Bilir, J.S. Harris, T.F. Jaramillo, Solar water splitting by photovoltaic-electrolysis with a solar-to-hydrogen efficiency over 30%, Nat. Commun. 7 (2016) 13237.

[8] S. Tembhurne, F. Nandjou, S. Haussener, A thermally synergistic photo-electrochemical hydrogen generator operating under concentrated solar irradiation, Nat. Energy 4 (2019) 399–407.

[9] W.J. Chang, K.-H. Lee, H. Ha, K. Jin, S.-T. Hwang, H.-m Lee, S.-W. Ahn, W. Yoon, H. Seo, J.S. Hong, Y.K. Go, J.-I. Ha, K.T. Nam, Design principle and loss engineering for photovoltaic–electrolysis cell system, ACS Omega 2 (2017) 1009–1018.

[10] J. Tournet, Y. Lee, S.K. Karuturi, H.H. Tan, C. Jagadish, III–V semiconductor materials for solar hydrogen production: status and prospects, ACS Energy Lett. 5 (2020) 611–622.

[11] J. Gao, F. Sahli, C. Liu, D. Ren, X. Guo, J. Werner, Q. Jeangros, S.M. Zakeeruddin, C. Ballif, M. Grätzel, J. Luo, Solar water splitting with perovskite/silicon tandem cell and TiC-supported Pt nanocluster electrocatalyst, Joule 3 (2019) 2930–2941.

[12] J. Luo, J.-H. Im, M.T. Mayer, M. Schreier, M.K. Nazeeruddin, N.-G. Park, S.D. Tilley, H.J. Fan, M. Grätzel, Water photolysis at 12.3% efficiency via perovskite photovoltaics and Earth-abundant catalysts, Science 345 (2014) 1593–1596.

[13] J. Werner, B. Niesen, C. Ballif, Perovskite/silicon tandem solar cells: marriage of convenience or true love story? – an overview, Adv. Mater. Interfaces 5 (2018), 1700731.

[14] A. Polman, M. Knight, E.C. Garnett, B. Ehrler, W.C. Sinke, Photovoltaic materials: present efficiencies and future challenges, Science (352) (2016) aad4424.

[15] K. Leo, Organic photovoltaics, Nat. Rev. Mater. 1 (2016) 16056.

[16] J.Y. Kim, K. Lee, N.E. Coates, D. Moses, T.-Q. Nguyen, M. Dante, A.J. Heeger, Efficient tandem polymer solar cells fabricated by all-solution processing, Science 317 (2007) 222.

[17] S. Hu, C. Xiang, S. Haussener, A.D. Berger, N.S. Lewis, An analysis of the optimal band gaps of light absorbers in integrated tandem photoelectrochemical water-splitting systems, Energy Environ. Sci. 6 (2013) 2984–2993.

[18] W. Lee, J. Yeop, J. Heo, Y.J. Yoon, S.Y. Park, J. Jeong, Y.S. Shin, J.W. Kim, N.G. An, D.S. Kim, J. Park, J.Y. Kim, High colloidal stability ZnO nanoparticles independent on solvent polarity and their application in polymer solar cells, Sci. Rep. 10 (2020) 18055.

[19] Y.K. Kim, J.H. Kim, Y.H. Jo, J.S. Lee, Precipitating metal nitrate deposition of amorphous metal oxyhydroxide electrodes containing Ni, Fe, and Co for electrocatalytic water oxidation, ACS Catal. 9 (2019) 9650–9662.

[20] C. Fan, D.L. Piron, A. Sleb, P. Paradis, Study of electrodeposited nickel-molybdenum, nickel-tungsten, cobalt-molybdenum, and cobalt-tungsten as hydrogen electrodes in alkaline water electrolysis, J. Electrochem. Soc. 141 (2019) 382–387.

[21] R.G. Milazzo, S.M.S. Privitera, D. D'Angelo, S. Scalese, S. Di Franco, F. Maita, S. Lombardo, Spontaneous galvanic displacement of Pt nanostructures on nickel foam: synthesis, characterization and use for hydrogen evolution reaction, Int. J. Hydrog. Energy 43 (2018) 7903–7910.

[22] L. Tamasauskaite-Tamasiunaite, A. Zabielaite, A. Balciunaite, B. Sebeka, I. Stalnioniene, V. Buzas, L. Maciulis, L. Tumonis, E. Norkus, Deposition of Pt nanoparticles on Ni foam via galvanic displacement, ECS Trans. 72 (2016) 1–7.

[23] T.H. Lee, S.Y. Park, W.-W. Park, X. Du, J.H. Son, N. Li, O.-H. Kwon, H.Y. Woo, C.J. Brabec, J.Y. Kim, Efficient exciton diffusion in organic bilayer heterojunctions with nonfullerene small molecular acceptors, ACS Energy Lett. 5 (2020) 1628–1635.

[24] J. Wu, J. Lee, Y.-C. Chin, H. Yao, H. Cha, J. Luke, J. Hou, J.-S. Kim, J.R. Durrant, Exceptionally low charge trapping enables highly efficient organic bulk heterojunction solar cells, Energy Environ. Sci. 13 (2020) 2422–2430.

[25] S. Li, L. Ye, W. Zhao, S. Zhang, S. Mukherjee, H. Ade, J. Hou, Energy-level modulation of small-molecule electron acceptors to achieve over 12% efficiency in polymer solar cells, Adv. Mater. 28 (2016) 9423–9429.

[26] H. Zhang, S. Li, B. Xu, H. Yao, B. Yang, J. Hou, Fullerene-free polymer solar cell based on a polythiophene derivative with an unprecedented energy loss of less than 0.5 eV, J. Mater. Chem. A 4 (2016) 18043–18049.

[27] Q. Liu, Y. Jiang, K. Jin, J. Qin, J. Xu, W. Li, J. Xiong, J. Liu, Z. Xiao, K. Sun, S. Yang, X. Zhang, L. Ding, 18% efficiency organic solar cells, Sci. Bull. 65 (2020) 272–275.

[28] H. Aqoma, R. Azmi, S.-H. Oh, S.-Y. Jang, Solution-processed colloidal quantum dot/organic hybrid tandem photovoltaic devices with 8.3% efficiency, Nano Energy 31 (2017) 403–409.

[29] Z.W. Seh, J. Kibsgaard, C.F. Dickens, I. Chorkendorff, J.K. Nørskov, T.F. Jaramillo, Combining theory and experiment in electrocatalysis: insights into materials design, Science 355 (2017).

[30] I. Roger, M.A. Shipman, M.D. Symes, Earth-abundant catalysts for electrochemical and photoelectrochemical water splitting, Nat. Rev. Chem. 1 (2017) 0003.

[31] C.C.L. McCrory, S. Jung, J.C. Peters, T.F. Jaramillo, Benchmarking heterogeneous electrocatalysts for the oxygen evolution reaction, J. Am. Chem. Soc. 135 (2013) 16977–16987.

[32] X. Hu, X. Tian, Y.-W. Lin, Z. Wang, Nickel foam and stainless steel mesh as electrocatalysts for hydrogen evolution reaction, oxygen evolution reaction and overall water splitting in alkaline media, RSC Adv. 9 (2019) 31563–31571.

[33] S. Anantharaj, S.R. Ede, K. Karthick, S. Sam Sankar, K. Sangeetha, P.E. Karthik, S. Kundu, Precision and correctness in the evaluation of electrocatalytic water splitting: revisiting activity parameters with a critical assessment, Energy Environ. Sci. 11 (2018) 744–771.

[34] Y. Chen, F. Mojica, G. Li, P.-Y.A. Chuang, Experimental study and analytical modeling of an alkaline water electrolysis cell, Int. J. Energy Res. 41 (2017) 2365–2373.

[35] D.M.F. Santos, C.A.C. Sequeira, J.L. Figueiredo, Hydrogen production by alkaline water electrolysis, Quim. Nova 36 (2013) 1176–1193.

[36] M.T. Winkler, C.R. Cox, D.G. Nocera, T. Buonassisi, Modeling integrated photovoltaic–electrochemical devices using steady-state equivalent circuits, Proc. Natl. Acad. Sci. USA 110 (2013) E1076–E1082.

[37] L. Duan, A. Uddin, Progress in stability of organic solar cells, Adv. Sci. 7 (2020), 1903259.

[38] P. Cheng, X. Zhan, Stability of organic solar cells: challenges and strategies, Chem. Soc. Rev. 45 (2016) 2544–2582.

[39] L. Córcoles, J. Abad, J. Padilla, A. Urbina, Wavelength influence on the photodegradation of P3HT:PCBM organic solar cells, Sol. Energy Mater. Sol. Cells 141 (2015) 423–428.

[40] Y. Zhao, Z. Wu, X. Liu, Z. Zhong, R. Zhu, J. Yu, Revealing the photo-degradation mechanism of PM6:Y6 based high-efficiency organic solar cells, J. Mater. Chem. C 9 (2021) 13972–13980.

[41] J.M. Yu, J. Lee, Y.S. Kim, J. Song, J. Oh, S.M. Lee, M. Jeong, Y. Kim, J.H. Kwak, S. Cho, C. Yang, J.-W. Jang, High-performance and stable photoelectrochemical water splitting cell with organic-photoactive-layer-based photoanode, Nat. Commun. 11 (2020) 5509.

[42] H. Kimura, K. Fukuda, H. Jinno, S. Park, M. Saito, I. Osaka, K. Takimiya, S. Umezu, T. Someya, High operation stability of ultraflexible organic solar cells with ultraviolet-filtering substrates, Adv. Mater. 31 (2019), 1808033.

[43] A. Weu, J.A. Kress, F. Paulus, D. Becker-Koch, V. Lami, A.A. Bakulin, Y. Vaynzof, Oxygen-induced doping as a degradation mechanism in highly efficient organic solar cells, ACS Appl. Energy Mater. 2 (2019) 1943–1950.

[44] S.Y. Reece, J.A. Hamel, K. Sung, T.D. Jarvi, A.J. Esswein, J.J.H. Pijpers, D. G. Nocera, Wireless solar water splitting using silicon-based semiconductors and earth-abundant catalysts, Science 334 (2011) 645.

[45] J.H. Kim, Y. Jo, J.H. Kim, J.W. Jang, H.J. Kang, Y.H. Lee, D.S. Kim, Y. Jun, J.S. Lee, Wireless solar water splitting device with robust cobalt-catalyzed, dual-doped BiVO4 photoanode and perovskite solar cell in tandem: a dual absorber artificial leaf, ACS Nano 9 (2015) 11820–11829.

[46] S. Esiner, H. van Eersel, G.W.P. van Pruissen, M. Turbiez, M.M. Wienk, R.A. J. Janssen, Water splitting with series-connected polymer solar cells, ACS Appl. Mater. Interfaces 8 (2016) 26972–26981.

[47] Q. Wu, J. Guo, R. Sun, J. Guo, S. Jia, Y. Li, J. Wang, J. Min, Slot-die printed non-fullerene organic solar cells with the highest efficiency of 12.9% for low-cost PV-driven water splitting, Nano Energy 61 (2019) 559–566.

[48] Y. Gao, V.M. Le Corre, A. Gaïtis, M. Neophytou, M.A. Hamid, K. Takanabe, P. M. Beaujuge, Homo-tandem polymer solar cells with VOC >1.8 V for efficient PV-driven water splitting, Adv. Mater. 28 (2016) 3366–3373.

[49] S. Esiner, G.W.P. van Pruissen, M.M. Wienk, R.A.J. Janssen, Optimized light-driven electrochemical water splitting with tandem polymer solar cells, J. Mater. Chem. A 4 (2016) 5107–5114.

[50] X. Elias, Q. Liu, C. Gimbert-Suriñach, R. Matheu, P. Mantilla-Perez, A. Martinez-Otero, X. Sala, J. Martorell, A. Llobet, Neutral water splitting catalysis with a high FF triple junction polymer cell, ACS Catal. 6 (2016) 3310–3316.

[51] S. Esiner, H. van Eersel, M.M. Wienk, R.A.J. Janssen, Triple junction polymer solar cells for photoelectrochemical water splitting, Adv. Mater. 25 (2013) 2932–2936.

[52] S. Esiner, R.E.M. Willems, A. Furlan, W. Li, M.M. Wienk, R.A.J. Janssen, Photoelectrochemical water splitting in an organic artificial leaf, J. Mater. Chem. A 3 (2015) 23936–23945.

[53] A. Ursua, L.M. Gandia, P. Sanchis, Hydrogen production from water electrolysis: current status and future trends, Proc. IEEE 100 (2012) 410–426.

[54] A. Rothschild, H. Dotan, Beating the efficiency of photovoltaics-powered electrolysis with tandem cell photoelectrolysis, ACS Energy Lett. 2 (2017) 45–51.